JCTC Journal of Chemical Theory and Computation

pubs.acs.org/JCTC Article

In Silico Study of a Bacteriorhodopsin/TiO_2 Hybrid System at the Molecular Level

Mayra Avelar,[#] Carmen Coppola, Alessio d'Ettorre,[#] Andrea Ienco, Maria Laura Parisi, Riccardo Basosi, Annalisa Santucci, Massimo Olivucci, and Adalgisa Sinicropi*

Cite This: *J. Chem. Theory Comput.* 2025, 21, 3231−3245 Read Online

ABSTRACT: Bacteriorhodopsin (bR) is a light-harvesting membrane protein that represents a promising sensitizer of TiO_2 for photovoltaic and photoelectrochemical devices. However, despite numerous experimental studies, the molecular-level understanding of the bR/TiO_2 hybrid system is still unsatisfactory. In this contribution, we report the construction and analysis of an atomistic model of such a system. To do so, both steered molecular dynamics-molecular dynamics and quantum mechanics/molecular mechanics computations are applied to four different bR orientations on the anatase TiO_2 surface. The resulting bR/TiO_2 models are then used to compute the light absorption maxima changes relative to those of bR. We show that all four models reproduce the experimentally observed blue-shift value induced by bR binding on TiO_2 and could be used to study the binding and binding-induced protein modifications. We conclude that the constructed models could provide a basis for future studies aiming to simulate the complex long-range electron transfer mechanism in bR/TiO_2-based solar energy conversion devices as well as in engineering bR to achieve enhanced efficiencies.

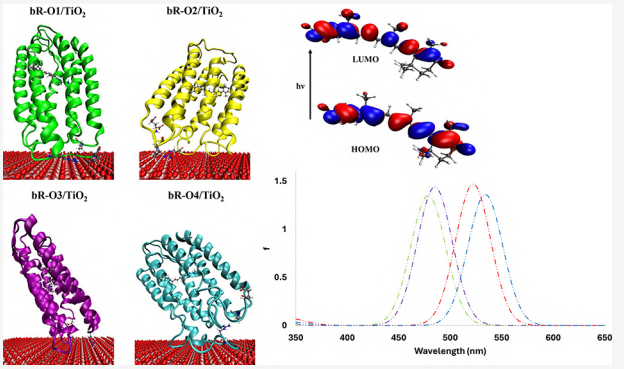

1. INTRODUCTION

Bacteriorhodopsin (bR) is a light-harvesting protein produced by *Halobacterium salinarum*,[1−3] formed by seven connected transmembrane alpha-helices incorporating a retinal chromophore bound to a lysine residue via a protonated Schiff's base linkage.[4−7] Upon absorption of a photon, bR enters a photocycle characterized by several intermediates with distinct absorption bands[8−11] and resulting in the transfer of a proton from the inner to the outer side of the cell membrane. The generated proton gradient is then exploited by the cell to generate chemical energy.

Due to its favorable properties, bR is a promising candidate for the construction of hybrid functional materials to be used in diverse applications. In fact, it is stable at temperatures over 80 °C in water and up to 140 °C in dry conditions, at high ionic strength (3 M NaCl), and over a wide pH range.[12−14] bR also exhibits a relatively broad absorption in the visible region, with a maximum at 568 and 553 nm in its trimeric and monomeric states, respectively, and a high quantum conversion efficiency (65%).[15,16] Several examples of bR-based functional materials have been patented or presented in the fields of bioelectronics,[17−19] biosensors,[20−22] optical memories,[14,23] hydrogen production,[24−27] bioremediation,[28] and solar cells.[29−37]

In solar energy conversion devices, bR has mainly been used as a TiO_2 sensitizer in photovoltaic (PV)[30,33−35,38−41] and photoelectrochemical (PEC)[24−27] cells to convert solar energy into electricity or chemical fuels (e.g., H_2), respectively. In terms of enhanced sustainability, bR appears as the candidate of choice. Indeed, unlike synthetic molecules, it is potentially highly available and could be easily extracted at a low cost for the fabrication of biodegradable devices.[31]

In the context of last-generation PV, Thavasi et al. reported the first case study of a biosensitized solar cell (BSSC) in which bR immobilized on TiO_2 was used as a photoanode.[38] Among several attempts to improve the photoconversion efficiency (η) of BSSCs,[30,31,33,34,39,41] the cosensitization with the green fluorescent protein, the chemical treatment with surfactants such as the nonionic Triton X-100 (that transforms the bR from its native trimeric state to a monomeric state), and the employment of an acetamide-based gel electrolyte instead of a triiodide-based electrolyte allowed to reach η = 0.40, 0.47, and 0.49%, respectively.[31,35,39] Moreover, BSSCs employing TiO_2 nanorods decorated with reduced graphene oxide (rGO) as photoanodes and sensitized with bR showed the highest

Received: October 13, 2024
Revised: January 27, 2025
Accepted: February 7, 2025
Published: March 4, 2025

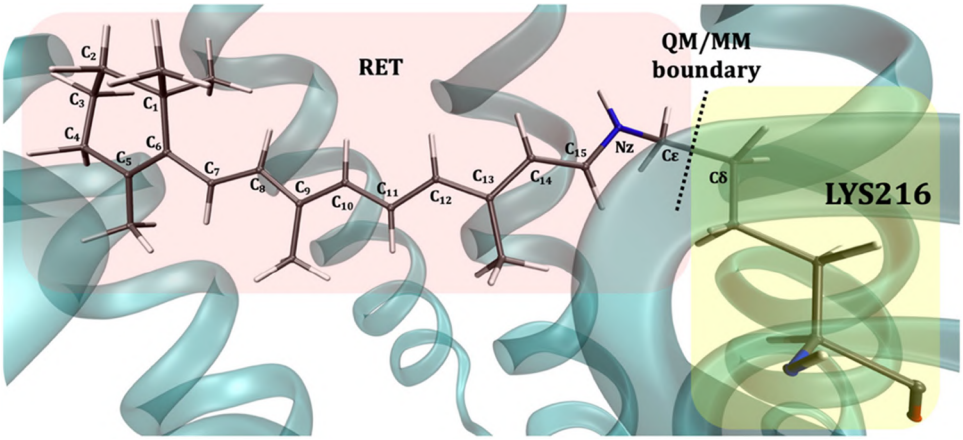

Figure 1. QM region (highlighted in the light red box) employed in the QM/MM calculations.

observed η value (1.32%).[34] In 2019, Das et al.[32] reported a perovskite solar cell (PSC) incorporating bR/TiO_2 layers. This bio-PSC (BPSC) showed significant improvement in η in comparison to PSCs without bR (17.0% vs 14.6%).

In the framework of PEC water splitting, the first report on PEC photoanodes composed of bR/TiO_2 nanotubes was published in 2011 by Allam et al., who demonstrated that the electrode allowed to reach a ca. 50% increase in photocurrent density with respect to that measured for pure TiO_2 nanotubes.[26] In order to enhance light-assisted water splitting, the bR was then investigated on different morphological TiO_2 substrates,[25] as well as when assembled on a Pt/TiO_2 nanocatalyst, showing to overcome the low stability and the structural complexity of other photocatalytic systems.[24] Another study reported that bR combined with reduced graphene oxide (rGO) was successfully introduced in the Pt/TiO_2 nanocatalyst, enhancing the photocurrent by collective charge injections while reducing the content of the Pt nanocatalyst.[42] Additionally, when encapsulated in titania gels, it was found an increase of 52% in hydrogen production compared to gels without the protein.[27]

In spite of the sizable body of work summarized above, there is still a lack of molecular level understanding of the bR/TiO_2 hybrid system. In fact, to the best of our knowledge, the interaction of bR with the photoactive anatase TiO_2 has not been investigated. This is why, here, we present a first computational study aimed at the construction and characterization of an atomistic model of bR/TiO_2 using a combination of steered molecular dynamics and molecular dynamics (SMD-MD) and quantum mechanics/molecular mechanics (QM/MM) calculations, somehow expanding other studies such as the recently reported molecular dynamics characterization of bR absorbed on a graphene sheet.[23]

As detailed below, we demonstrate that the resulting four different bR/TiO_2 models featuring distinct protein−surface orientations all yield wavelengths of the absorption maxima (λ^{a}_{max}) that are blue-shifted with respect to a consistent bR model. A comparison with experimentally observed spectral changes is used to validate and rank the models and, ultimately, to derive information about the binding.

2. COMPUTATIONAL DETAILS

2.1. QM/MM Simulations of Isolated bR. A monomeric, gas-phase, and globally uncharged QM/MM model of bR was built using the automatic rhodopsin modeling protocol (*a*-ARM), as described in ref 43 and starting from the protein's most recent crystallographic structure of *Halobacterium salinarum* (PDB ID: 6G7H).[10] The *a*-ARM bR model was then fully relaxed at a QM/MM level by using the CP2K 7.0 package.[44] The presently applied QM/MM scheme (see Figure 1) features a QM subsystem, including the retinal chromophore (RET) and atoms N_Z and C_ε of the covalently linked Lys216 side chain (along with their hydrogen atoms). The QM/MM boundary was set at the C_ε−C_δ bond of the same side chain and described using the hydrogen link-atom scheme (HLA).[45] The rest of the protein (backbone and side chains) and the crystallographic water molecules are included in the MM region. The QM region was treated at the density functional theory (DFT) level with the PBE exchange-correlation functional[46] and a double-ζ valence basis set with one polarization function (DZVP). The MM subsystem was instead treated with the CHARMM36 force field[47] using retinal parameters taken from the toppar_all36_prot_retinol.str library (www.charmm-gui.org). DFT calculations were performed employing the Quickstep[48] QM code of CP2K using a mixed Gaussian and plane-wave (GPW) approach and an auxiliary plane-wave basis for density with a cutoff of 350 Ry. The frontier was treated within the IMOMM link atom scheme[49] based on the generalized hybrid orbital (GHO) method.[50] Dual-space Gaussian-type pseudopotentials of Goedecker, Teter, and Hutter (GTH) optimized for the PBE functional were used to describe nuclei and core electrons.[51] From now on, such a QM/MM model will be called the PBE/CHARMM36 model.

2.2. Hybrid Steered Molecular Dynamics—Molecular Dynamics Simulations (SMD-MD) and QM/MM Simulations of bR/TiO_2 Hybrid Systems. To simulate the adsorption mechanism of bR on TiO_2, the anatase surface was adopted since, among mesoporous and crystalline (brookite, rutile, and anatase phases) TiO_2, it is the most used in photocatalysis.[52−54] For instance, Jeganathan et al.[33] reported that a BSSC built with bR and anatase TiO_2 nanorods showed a conversion efficiency of 0.84% superior to the 0.72% obtained using rutile TiO_2 nanorods.

The anatase surface was modelized with a total of 12276 atoms corresponding to three layers on the *c*-axis and an area of 115 × 115 Å^2.

Insights from previous experimental studies reported that the immobilization of bR and its orientation onto the TiO_2 surface are key factors affecting the devices' performance.[26,38]

https://doi.org/10.1021/acs.jctc.4c01370
J. Chem. Theory Comput. 2025, 21, 3231−3245

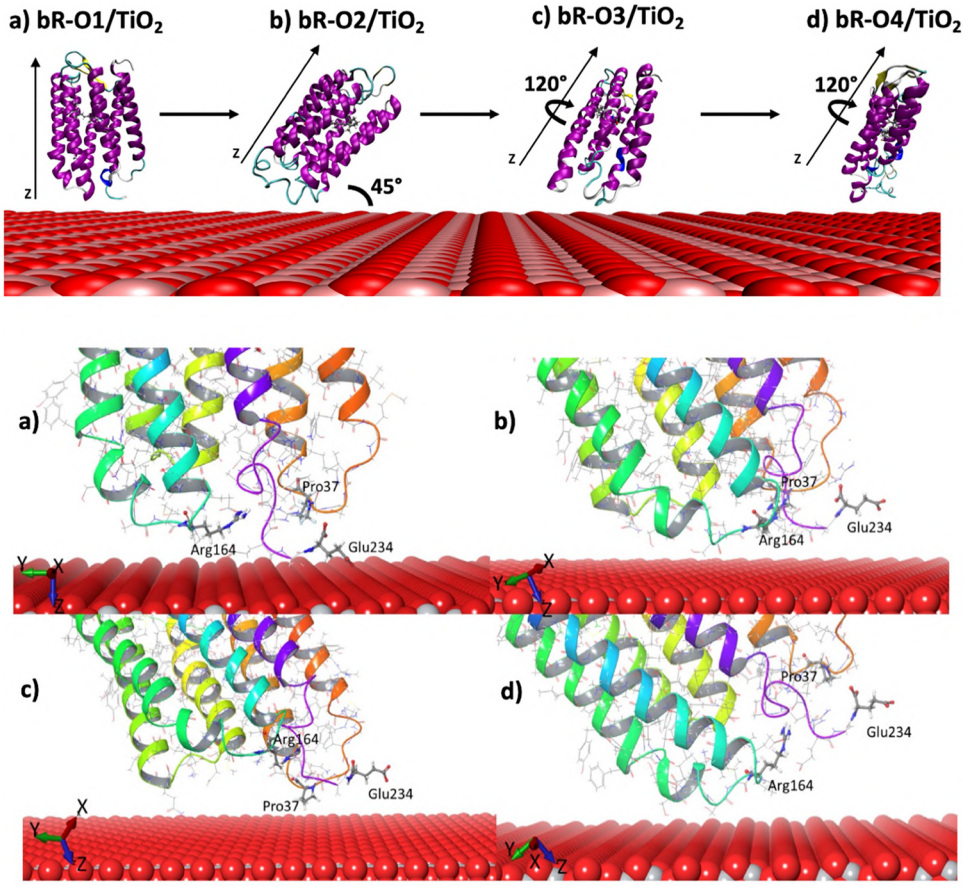

Figure 2. Top: tilting and rotating directions used to generate (a) **bR-O1**/TiO_2, (b) **bR-O2**/TiO_2, (c) **bR-O3**/TiO_2, and (d) **bR-O4**/TiO_2 systems. Bottom: zoom of the protein structures of **bR-O1**/TiO_2, **bR-O2**/TiO_2, **bR-O3**/TiO_2, and **bR-O4**/TiO_2 in the proximity of the surface. Models were created using MAESTRO 11.8 Schrödinger Release 2020−1: Maestro, Schrödinger, LLC, New York, NY, 2020).[57] The anatase surface is shown in a ball and stick representation (gray balls represent titanium atoms, whereas red balls represent oxygen atoms). The protein is reported in its secondary structure, and residues Pro37, Arg164, and Glu234 are displayed in ball and stick representation.

In light of this, the geometrically relaxed PBE/CHARMM36 optimized bR model was placed on the anatase surface in four different orientations and, therefore, types of bR/surface contacts, labeled as **bR-O1**/TiO_2, **bR-O2**/TiO_2, **bR-O3**/TiO_2, and **bR-O4**/TiO_2. More specifically, the bR axis (i.e., the axis roughly parallel to the α-helices, also indicated as the z-axis) was placed in a perpendicular orientation with respect to the anatase surface in **bR-O1**/TiO_2 (Figure 2a), while the **bR-O2**/TiO_2, **bR-O3**/TiO_2, and **bR-O4**/TiO_2 systems (Figure 2b−d) were obtained by tilting the perpendicularly oriented **bR-O1**/TiO_2 by 45° on the xy plane and then rotating by 120° around the z-axis (see Figure 2, top). The SMD-MD simulations were thus carried out setting, in all models, the initial position of the bR at a distance of 5 Å from the TiO_2 surface. In all cases, the initial orientations were set at the C-terminus since this face poses more charged residues (Asp, Glu, Arg, Lys) than the N-terminus, thus allowing a more favorable interaction.[33,38] In particular, the positively charged Arg and Lys residues are already known to be potential binding groups on TiO_2.[38,55,56] Furthermore, the four orientations involve the interactions of all the helices of the C-terminus tail of bR with TiO_2, and thus they could be considered representative of the physisorption mode at the C-terminus region.

All SMD-MD simulations were carried out using the NAMD 2.12 code[58] with the CHARMM36 force field,[47,59−61] a protocol commonly adopted in literature.[62−64] The TiO_2 was described by the Lennard-Jones parameters from Brandt and Lyubartsev.[65] Calculations were performed at 300 K in the NVT ensemble (Langevin dynamics) with a cutoff of 12 Å for nonbonded interactions. Long-range electrostatic interactions were modeled with Particle Mesh Ewald (PME) and periodic boundary conditions (PBC) were applied.

To stabilize the thermodynamic properties, after the energy minimization, an equilibration step was performed via a 200 ps MD simulation for each bR/TiO_2 hybrid system, keeping the protein backbone and the surface fixed. After the equilibration step, a 500 ps SMD simulation was applied to accelerate the protein−surface adsorption process, with the TiO_2 surface kept fixed. SMD calculations were performed with a constant velocity of the pulling atoms (the backbone of bR) of 1×10^{-6} Å/ps and a spring constant of 5 kcal/mol $Å^2$.[62−64] The magnitude of these constants is comparable to or lower than those reported in the literature for similar systems,[62−64] and they were chosen to avoid undesired artificial denaturation of the protein and its active site. The final structures of bR/TiO_2 systems from SMD simulations were used for 7.5 ns MD simulations with a 1 fs time step and rigid bonds for water molecules. For both SMD and MD simulations, harmonic restraints with a 1 kcal/mol $Å^2$ force constant were applied to all of the atoms of the retinal. Finally, protein desorption was done by performing a 2.0 ns SMD simulation for each bR/

https://doi.org/10.1021/acs.jctc.4c01370
J. Chem. Theory Comput. 2025, 21, 3231−3245

Table 1. TD-DFT Absorption Maxima (λ^{a}_{max}), Vertical Excitation Energies (E_{exc}), Oscillator Strengths (f), and Orbital Transition Contribution (%) for the Lowest Singlet−Singlet Excitation ($S_0 \rightarrow S_1$)[a] of Isolated bR Calculated with Different Functionals and the 6-31+G(d) Basis Set within the ONIOM-EE Scheme

	λ^{a}_{max} (nm)	E_{exc} (eV)	f	contrib. (%)	$\Delta E_{comp-exp}$ (eV)[b]
CAM-B3LYP	566	2.19	1.5	96% H → L	0.05[(a)]−0.01[(b)]
PBE0	578	2.15	0.67	53% H → L	0.09[(a)]−0.03[(b)]
				30% H-3 → L	
LC-wPBE	562	2.21	1.6	91% H → L	0.03[(a)]−0.03[(b)]
M06-2X	577	2.15	1.5	98% H → L	0.09[(a)]−0.03[(b)]
bR from ref 73	491	2.53			
Experimental	568[(a)]	2.18[(a)]			
	553[(b)]	2.24[(b)]			

[a]Only for PBE0, the transition is $S_0 \rightarrow S_2$. [b]Energy differences between computed values and experimental ones for (a) the native trimeric state (2.18 eV)[15,26,35,79−81] and (b) the monomeric state (2.24 eV)[15,35,77,78] of bR.

TiO_2 hybrid system with a constant velocity of 5×10^{-5} Å/ps and a 50 kcal/mol Å^2 spring constant.[62−64]

Root mean square deviations (RMSD) and electrostatic energy interactions were computed using VMD 1.9.3.[66] All structures produced by the SMD-MD simulations and the isolated bR were subjected to QM/MM minimization using the CP2K software.[44] During minimization, the TiO_2 surface was maintained fixed. The QM/MM scheme features a QM subsystem including the retinal chromophore (RET), atoms N_z and C_ε of the covalently linked Lys216 side chain (along with their hydrogen atoms), Arg82, Tyr83, Ala84, Asp85, Trp86, Leu87, Phe88, Thr89, Trp138, Ala139, Ile140, Ser141, Thr142, Trp182, Ser183, Ala184, Tyr185, Pro186, Glu204 residues, and 8 TIP3 water molecules. The QM/MM boundary was set at the $C_\varepsilon-C_\delta$ bond of the Lys216 side chain and the $C-C_\alpha$ bonds of the residues located on the boundary. All of them were described using the hydrogen link-atom scheme (HLA).[45] The rest of the protein (backbone and side chains), the crystallographic water molecules, and the TiO_2 surface are included in the MM region.

2.3. Vertical Excitation Energy Calculations. Vertical excitation energy calculations were performed at the TD-DFT level using the ONIOM-EE (electrostatic embedding) method, as implemented in Gaussian 16, Revision C.01 suite of programs.[67] Two-layer (QM:MM) calculation schemes were used for the isolated bR and bR/TiO_2 systems. In both cases, the QM (high layer) region includes the retinal chromophore, Lys216, Arg82, Tyr83, Ala84, Asp85, Trp86, Leu87, Phe88, Thr89, Trp138, Ala139, Ile140, Ser141, Thr142, Trp182, Ser183, Ala184, Tyr185, Pro186, Glu204 residues, and 8 TIP3 water molecules. The MM (low layer) region includes the rest of the protein and crystallographic water molecules. For bR/TiO_2 systems, the MM region also includes the anatase TiO_2 surface. The QM/MM boundary was set at the $C_\varepsilon-C_\delta$ bond of the Lys216 side chain and the $C-C_\alpha$ bonds of the residues located on the boundary. The vertical excitation energies of the isolated bR were calculated employing CAM-B3LYP,[68] PBE0,[69] LC-wPBE,[70] and M06-2X[71] functionals, while those of **bR-O1**/TiO_2, **bR-O2**/TiO_2, **bR-O3**/TiO_2, and **bR-O4**/TiO_2 were obtained using M06-2X[71] and CAM-B3LYP[68] functionals. In both cases, the 6-31+G(d) basis set was adopted. The MM system was modeled using the AMBER force-field,[72] since it is the only adequate force field available in Gaussian 16 and following the work of Vreven & Morokuma.[73] For the retinal, parameters were taken from Melaccio et al.[74] To accurately describe the QM/MM edge, the point charges at the frontier atoms were taken from Andruniów et al.,[75] and they are reported in Table S1. The UV−Vis spectra were plotted with Molden 5.6[76] considering a 20 nm half-width and a Gaussian line shape. M06-2X/6-31+G(d) and CAM-B3LYP/6-31+G(d) levels of theory were also employed to calculate the vertical excitation energies of the isolated retinal chromophore taken with its protein bR equilibrium geometry ("bare chromophore").

3. RESULTS AND DISCUSSION

3.1. UV−Vis Vertical Excitation Properties of the Isolated bR. TD-DFT absorption maxima (λ^{a}_{max}), vertical excitation energies (E_{exc}), oscillator strengths (f), and composition (%) in terms of molecular orbitals (MOs) for the lowest singlet−singlet $S_0 \rightarrow S_1$ transition of the isolated bR calculated with the electrostatic embedding (ONIOM-EE) scheme and with the CAM-B3LYP, PBE0, LC-wPBE, and M06-2X functionals are presented in Table 1. The isolated bR (this is not to be confused with the isolated bR chromophore) shows an absorption maximum between 562 and 578 nm, corresponding to 2.21−2.15 eV. Looking at the wave function plot of molecular orbitals involved in the lowest energy transition (Figure 3), it is evident that the $S_0 \rightarrow S_1$ excitation is mainly characterized, not surprisingly, by a $\pi \rightarrow \pi^*$ transition which involves HOMO → LUMO orbitals.

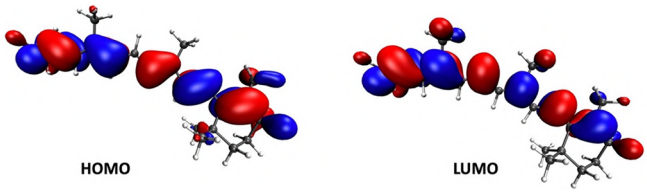

Figure 3. DFT-PBE/DZVP HOMO and LUMO of the retinal in isolated bR.

The computed values are in line with the experimental absorption maxima of bR with maximum energy differences of 0.09 and 0.03 eV, compared to the values reported for the native trimeric (2.18 eV) and monomeric (2.24 eV) states, respectively.[15,26,35,77−81] All of the tested functionals reproduce the experimental absorption value with similar accuracy. It should be noted that, in this work, the gauge invariance is not imposed for the M06-2X functional since the $S_0 \rightarrow S_1$ excitation of the isolated bR is associated with a $\pi \rightarrow \pi_{||}^*$ transition localized along the retinal conjugated chain that does not have a rotational displacement of occupied and virtual

https://doi.org/10.1021/acs.jctc.4c01370
J. Chem. Theory Comput. 2025, 21, 3231−3245

Table 2. Interaction Energies of bR-O1/TiO_2, bR-O2/TiO_2, bR-O3/TiO_2, and bR-O4/TiO_2

system	E_{int}[a] (kcal mol^{-1})	electrostatic energy (kcal mol^{-1})	vdW energy (kcal mol^{-1})
bR-O1/TiO_2	−135.3; σ = 7.2%	−92.6	−42.7
bR-O2/TiO_2	−134.1; σ = 7.3%	−106.1	−28.0
bR-O3/TiO_2	−134.4; σ = 6.5%	−128.5	−5.9
bR-O4/TiO_2	−282.3; σ = 8.3%	−211.4	−70.9

[a]The interaction energy corresponds to the sum of electrostatic and vdW energies as calculated using the NAMD plugin on VMD 1.9.3.[58] σ represents the standard deviation, expressed as a percentage of the mean.

Table 3. Interaction Energies, Number of Contact Atoms, and Interacting Amino Acids of bR-O1/TiO_2, bR-O2/TiO_2, bR-O3/TiO_2, and bR-O4/TiO_2 after SMD-MD Simulations

system	E_{int}[a] (kcal mol^{-1})	N. contacts[b]	residues[c]
bR-O1/TiO_2	−135.3 σ = 7.2%	145 ± 6	Ser35, Pro37, Asp102, **Lys159**, Ser162, Met163, **Arg164**, Pro165, **Arg227**, Ala228, Ile229, Phe230, Gly231, Glu232, Ala233, Glu234
bR-O2/TiO_2	−134.1 σ = 7.3%	121 ± 9	Pro37, Asp102, Ala103, Asp104, Gln105, Thr157, Ser158, **Lys159**, Ser162, Met163, **Arg164**, Pro165, Glu232
bR-O3/TiO_2	−134.4 σ = 6.5%	82 ± 9	Asp36, Pro37, Asp38, **Lys40**, **Lys41**, Phe42, Asp104, Gln105, **Arg164**
bR-O4/TiO_2	−282.3 σ = 8.3%	205 ± 10	Thr157, Ser158, **Lys159**, Glu161, Ser162, Met163, **Arg164**, Pro165, Glu166, Val167, Ala168, Ser169, Thr170, **Lys172**, Val173, Leu174, **Arg175**, **Arg225**

[a]Average energy during adsorption process (last 2 ns of MD simulation, corresponding to the interaction energy of Table 3). [b]Number of contacts taken as the average over the last 500 ps. [c]Adsorbed residues considered within 5 Å from the anatase surface. σ represents the standard deviation, expressed as a percentage of the mean.

orbitals (Figure 3), and it is, therefore, less sensitive to the gauge invariance correction, as reported in ref 82.

The absorption maxima values calculated here are compared to that (2.53 eV) previously calculated at ONIOM-(B3LYP:Amber)-EE level of theory in ref 73 (Table 1).

The analysis of the computed Kohn−Sham orbital energies reveals that the HOMO and LUMO energies of isolated bR are located at −4.7 and −3.4 eV, respectively, which are in fair agreement with those experimentally determined (−5.4 and −3.8 eV).[26,31] Given the favorable position of the bR LUMO relative to the conduction band of TiO_2 (−4.2 eV), we could assume a feasible electron injection, as usually reported in the literature for PV and PEC applications.[26,31]

3.2. Interaction Mechanism of bR-O1/TiO_2, bR-O2/TiO_2, bR-O3/TiO_2, and bR-O4/TiO_2. The results reported in Section 3.1 support the validity of our model of isolated bR. Such a model was therefore used to investigate the mechanism of the anatase TiO_2 adsorption. All the four investigated hybrid systems (**bR-O1**/TiO_2, **bR-O2**/TiO_2, **bR-O3**/TiO_2, and **bR-O4**/TiO_2) showed bR adsorption patterns on the anatase TiO_2 surface in nanoseconds (8 ns simulation recorded), which was considered an adequate time for describing the initial adsorption, as previously reported by Utesch et al.[62] As mentioned above, the initial orientations were set at the C-terminus of bR and in contact with the anatase TiO_2 surface.

In the SMD-MD approach, the peptides were steered toward the surface with a constant force applied to them. This computational methodology was successfully applied in previous works to investigate the adsorption and desorption mechanisms of bovine serum albumin (BSA), lysozyme, BMP-2 homodimer, and spectrin proteins on different implant surfaces.[62−64] To preserve the retinal conformation during the adsorption step (SMD-MD simulation), its geometry was restrained against the pulling forces by applying a harmonic restraint of 1 kcal/mol Å^2 to all its atoms. After SMD-MD simulations, the contact surface area between the protein and anatase was stabilized by electrostatic interactions among the charged amino acids at the C-terminus and the surface. The interaction energies of **bR-O1**/TiO_2, **bR-O2**/TiO_2, **bR-O3**/TiO_2, and **bR-O4**/TiO_2 systems, calculated as the average of the last 2 ns MD simulation, are reported in Table 2 along with their electrostatic and van der Waals components. We would like to clarify that the interaction energy calculated in this work refers only to the portion of the protein adsorbed to the anatase surface (within <5 Å from the surface), and, therefore, it comprehends a different number of atoms for each bR/TiO_2 model. Thus, this energy should not be confused with the total energy of the entire system. The distance cutoff at 5 Å has been selected based on previous works[23,62] and it allowed us to differentiate between the interaction energy caused by the residues in direct contact with the surface—which are responsible for the adsorption mechanism—and the interaction energy from the rest of the protein, which contributes only minimally. In the framework of this work, the chosen cutoff allows us to focus our attention on the first contribution, i.e., the interaction energy at the interface.

As reported in Table 2, the four bR/TiO_2 hybrid systems exhibit favorable (negative) interaction energies[62] (electrostatics + vdW) ranging between −134.1 kcal/mol of **bR-O2**/TiO_2 and −282.3 kcal/mol of **bR-O4**/TiO_2 (see also Figure S1). The trend of the interaction energies with respect to different cutoff distances has been investigated to rule out artifacts (Figure S2), and it is possible to notice that after 5 Å, it does not vary (**bR-O4**/TiO_2 with the lowest interaction energy and **bR-O1**/TiO_2, **bR-O2**/TiO_2, and **bR-O3**/TiO_2 with comparable interaction energies). Also notice that the electrostatic component is the main contributor to the interaction energy in all the bR/TiO_2 systems, suggesting that, during the adsorption process, the electrostatic interactions among the charged residues (Lys, Arg, Glu, and Asp) and the TiO_2 atoms predominate. On the other hand, the van der Waals energy depends on the number of contacts between the protein and the surface; hence, the lower the vdW energy, the higher the number of expected contacts.[62] The number of contacts for each cutoff distance increases similarly among the systems (Figure S3), and after 5 Å, at each cutoff distance, the percentage of newly formed contacts remains constant across the bR/TiO_2 systems.

https://doi.org/10.1021/acs.jctc.4c01370
J. Chem. Theory Comput. 2025, 21, 3231−3245

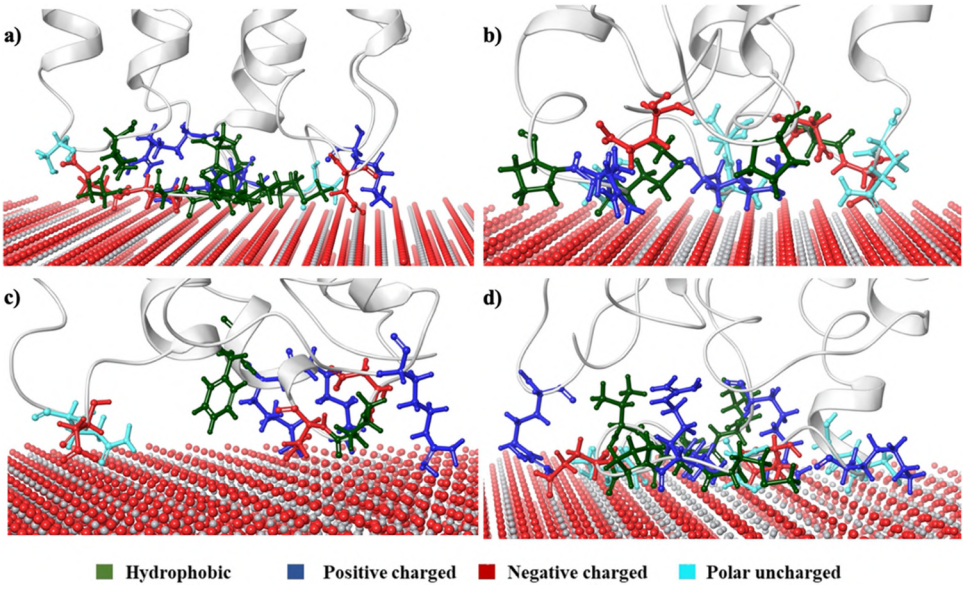

Figure 4. Interacting residues within 5 Å from the surface in (a) **bR-O1**/TiO_2, (b) **bR-O2**/TiO_2, (c) **bR-O3**/TiO_2, and (d) **bR-O4**/TiO_2 systems. Atom color scheme by residue property: dark green, hydrophobic; cyan, polar uncharged; blue, positively charged; red, negatively charged. The secondary structure is shown in gray. Models were created using MAESTRO 11.8 (Schrödinger Release 2020−1: Maestro, Schrödinger, LLC, New York, NY, 2020).[57]

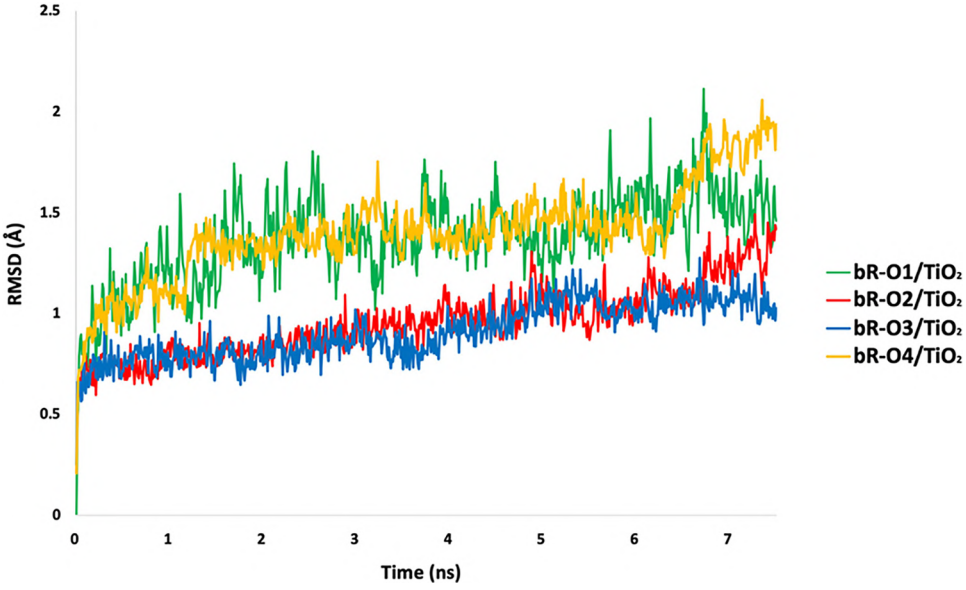

Figure 5. Backbone RMSD, in Å, of the four bR/TiO_2 hybrid systems during 7.5 ns of the MD adsorption process.

To gain further insights into the origin of these interactions and identify the amino acids in direct contact with the surface, we looked at the structures of the four bR/TiO_2 hybrid systems (Table 3 and Figure 4) including the number of contact atoms, i.e., the number of protein atoms within 5 Å from the anatase TiO_2 surface. They were taken as the average over the last 500 ps of MD simulations, and they are reported in Table 3.

At the interface of **bR-O2**/TiO_2, **bR-O3**/TiO_2, and **bR-O4**/TiO_2, charged and polar residues predominate, while almost the same number of charged/polar and hydrophobic residues are found at the **bR-O1**/TiO_2 interface (Table 3 and Figure 4). Since positively charged residues are known to be potential binding groups on TiO_2,[38,55,56] their presence at the interface of bR/TiO_2 hybrid systems (Table 3) promotes the covalent immobilization of bR onto the anatase surface. Furthermore, the highest number of contacts (205 ± 10) is present at the interface of **bR-O4**/TiO_2, while the lowest number of contacts (82 ± 10) is found in **bR-O3**/TiO_2 (Table 3). Indeed, these two hybrid systems exhibit the lowest and highest values of vdW energy, respectively. Based on these results, we conclude that the lowest energy of **bR-O4**/TiO_2 could be ascribed to both the number of contacts and the type of interacting residues.

The structural stability of the bR/TiO_2 hybrid systems was measured by means of the RMSD and is reported in Figure 5. The backbone RMSD of **bR-O2**/TiO_2 and **bR-O3**/TiO_2 consistently fluctuates around 0.9 Å, while that of **bR-O1**/TiO_2 and **bR-O4**/TiO_2 regularly oscillates around 1.4 Å, suggesting that the secondary structure (α-helix, 3_{10}-helix, and

https://doi.org/10.1021/acs.jctc.4c01370
J. Chem. Theory Comput. 2025, 21, 3231−3245

Table 4. Secondary Structure (%) of bR-O1/TiO_2, bR-O2/TiO_2, bR-O3/TiO_2, and bR-O4/TiO_2 after SMD-MD Simulations[a]

	bR[b]	bR-O1/TiO_2	bR-O2/TiO_2	bR-O3/TiO_2	bR-O4/TiO_2
α-helix	76.1	69.6	67.0	66.1	61.3
3_{10}-helix	1.3	0.0	1.7	2.2	3.0
β-sheet	4.3	1.7	0.0	1.7	4.8
total	81.7	71.3	68.7	70.0	69.1

[a]bR initial structure is shown for comparison. [b]CP2K QM/MM optimized geometry.

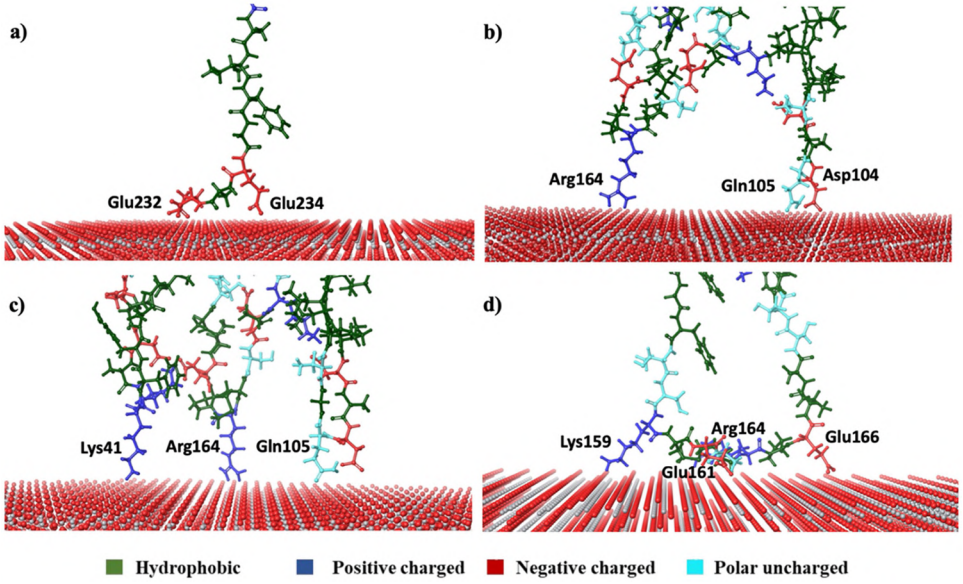

Figure 6. Representation of the last interacting residues of the desorption process in (a) **bR-O1**/TiO_2, (b) **bR-O2**/TiO_2, (c) **bR-O3**/TiO_2, and (d) **bR-O4**/TiO_2 systems. Atom color scheme by residue property: dark green, hydrophobic; cyan, polar uncharged; blue, positively charged; red, negatively charged. Models were created using MAESTRO 11.8 (Schrödinger Release 2020−1: Maestro, Schrödinger, LLC, New York, NY, 2020).[57]

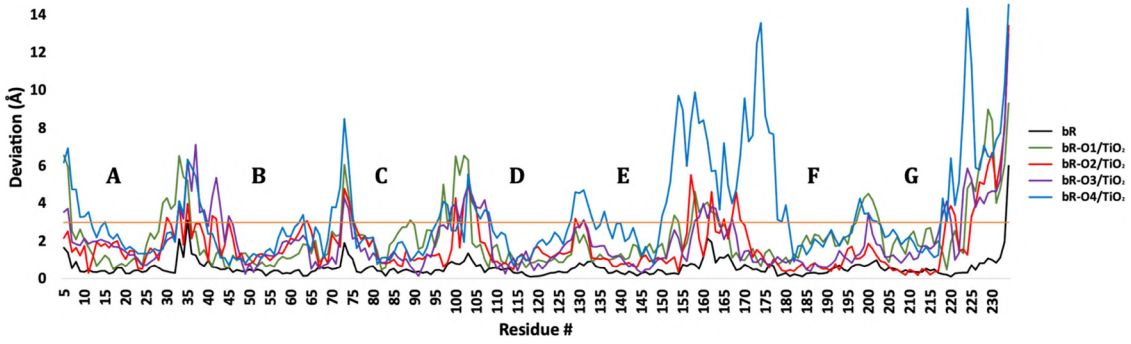

Figure 7. Deviations of C−α coordinates of the optimized isolated bR and **bR-O1**/TiO_2, **bR-O2**/TiO_2, **bR-O3**/TiO_2, and **bR-O4**/TiO_2 systems with respect to the bR crystallographic structure.

β-sheet) of all of the bR/TiO_2 hybrid systems is marginally affected during the interaction with the surface. Indeed, the loss in the secondary structure is predicted to be 10.4, 13.0, 11.7, and 12.6% for **bR-O1**/TiO_2, **bR-O2**/TiO_2, **bR-O3**/TiO_2, and **bR-O4**/TiO_2 with respect to that of the isolated bR (Table 4). Moreover, it is interesting to notice that the residues that lose the secondary structure are mostly those near the anatase surface, revealing that the observed loss can be ascribed to the protein−surface interactions and is not related to the forces applied to push the protein on the surface. In particular, at the end of the simulation, it is possible to notice that the RMSD of **bR-O4**/TiO_2 has a little increase related to the adsorption of two residues on the TiO_2 surface. Indeed, the hydrogen atoms of Arg175 and Lys159 play a role in forming hydrogen bonds with the oxygen atoms on the surface. After ca. 6.50 ns of MD simulation, the H_{H11} of Arg175, which was previously at an average distance of 4.87 Å from the O_{6399} of TiO_2, forms a hydrogen bond at 1.70 Å (average distance over the last ns). Similarly, the H_{Z3} of Lys159, which was initially found at an average distance of 2.93 Å from the O_{6536} of TiO_2, forms a hydrogen bond at 1.50 Å (average distance over the last ns), as also shown in Figure S4. A total decrease of about 40 kcal/mol (ca. 20 kcal/mol for the H_{H11} of Arg175 and ca. 15 kcal/mol for H_{Z3} of Lys159) in the interaction energy is found. On the other hand, the small change in the RMSD (an increase of 0.2 Å) found at the end of the **bR-O2**/TiO_2

https://doi.org/10.1021/acs.jctc.4c01370
J. Chem. Theory Comput. 2025, 21, 3231−3245

simulation cannot be ascribed to the adsorption of single residues but is related to Pro37 approaching the surface. It corresponds to an increase of ca. 4 kcal/mol in the electrostatic energy (see Figure S1).

To investigate the amino acids responsible for the strongest interactions at the bR/TiO_2 interface, the bR was pulled away from the anatase surface in all the analyzed hybrid systems by applying an external force greater than the one used for the adsorption process. A complete desorption is defined as zero electrostatic and vdW interactions between bR and the anatase TiO_2 surface. Figure 6 shows the last interacting amino acids of the desorption process, which are Glu232 and Glu234 in **bR-O1**/TiO_2 (Figure 6a), Asp104, Gln105, and Arg164 in **bR-O2**/TiO_2 (Figure 6b), Lys41, Gln105, and Arg164 in **bR-O3**/TiO_2 (Figure 6c), and Lys159, Glu161, Arg164, and Glu166 in **bR-O4**/TiO_2 (Figure 6d).

3.3. QM/MM Minimization of bR-O1/TiO_2, bR-O2/TiO_2, bR-O3/TiO_2, and bR-O4/TiO_2 Systems. The four bR/TiO_2 hybrid systems were then subjected to a QM/MM optimization. After optimization, a thorough analysis of all relevant parameters (deviation of C−α coordinates, bond length distances, bond length alternation (BLA), positive charge distribution, and dihedral angle values) was carried out to ensure that the structure of the protein remains unaffected during the optimization process across all considered systems. Indeed, we aimed to demonstrate that the retinal chromophore can retain its functions after the adsorption process. Deviations of the C−α coordinates for the optimized isolated bR and bR/TiO_2 hybrid systems with respect to the crystallographic structure are reported in Figure 7.

Figure 7 displays seven valleys, here indicated with letters from A to G, that correspond to the protein α-helices and eight peaks among the valleys that correspond to the loops. Focusing our attention on the helices, we can observe a deviation lower than 1 Å from the crystallographic values for the optimized isolated bR (black line in Figure 7), indicating that the optimized structure is very similar to the crystallographic one.

Slightly higher deviations are found for the optimized hybrid bR/TiO_2 systems due to MD simulations. Anyway, since only a few C−α atoms deviate more than 3 Å (see the orange line in Figure 7), it is possible to conclude that the four structures are likewise preserved after optimization. As expected, the highest deviation is observed between helices E and F, particularly from residue 150 to residue 177, and mostly for **bR-O4**/TiO_2 (average deviation of 7.2 Å). Indeed, this corresponds to the portion of the protein adsorbed on TiO_2 (see also the interacting amino acids in Table 3), which loses its helix-like structure. Moreover, we can observe that a deviation higher than 3 Å is also found in the last 15 residues (the protein C-terminus tail, the one closer to the surface during SMD-MD), and it is attributed to two distinct factors. The first is related to the higher mobility of the C-terminus tail's residues compared to the others, and the second is ascribed to the adsorption process and the subsequent contact of the residues with the surface. Indeed, only the first factor is present in the optimized bR model.

Additionally, considering the role of the retinal chromophore cavity in the bR functionality, the deviations of the residues in the cavity environment of the retinal were carefully analyzed. The representation of the chromophore and its surrounding residues is reported in Figure 8.

Deviations of the C−α coordinates of amino acids present in the cavity of the optimized isolated bR and the hybrid bR/TiO_2 systems with respect to the crystallographic structure are reported in Figure 9. We can observe an average deviation of 0.3 Å from the crystallographic values for the optimized isolated bR, while an average deviation of less than 1.7 Å is found for the amino acids within the cavity of the optimized bR/TiO_2 systems. The Thr89 of **bR-O1**/TiO_2 shows the highest deviation at 3.1 Å. Hence, the tertiary structure of the protein is not affected by the optimization process in all the considered systems, and one can tentatively hypothesize that the active center, i.e., the chromophore, and its environment preserve their functions.

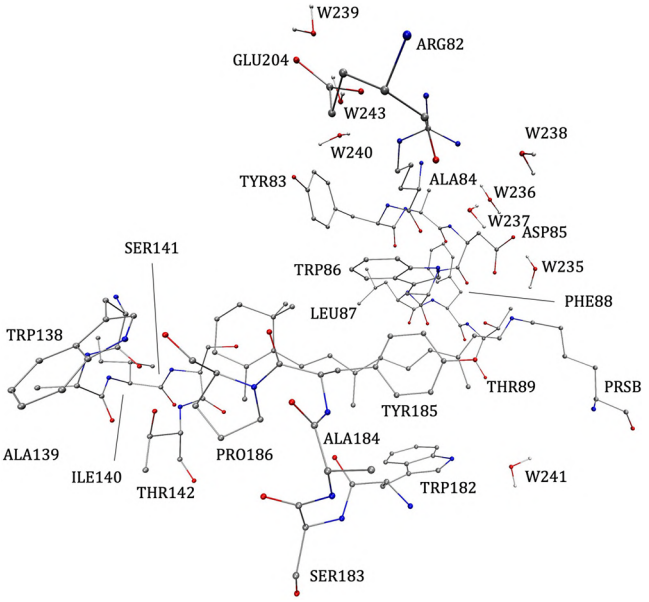

Figure 8. Representation of the cavity environment. Only hydrogens of water molecules are reported explicitly.

To further support the above hypothesis, an in-depth analysis of the retinal optimized geometries in the four bR/TiO_2 systems was then carried out. In particular, the bond length distances (Figure 10), the positive charge distribution (Figure 11), and the dihedral angles (Figure 12) along the retinal conjugated chain of **bR-O1**/TiO_2, **bR-O2**/TiO_2, **bR-O3**/TiO_2, and **bR-O4**/TiO_2 are reported in comparison to those of the retinal in the QM/MM optimized isolated bR. Bond lengths and dihedral angle values were also compared to those calculated using the ONIOM(B3LYP:Amber)-EE methodology in the work of Vreven & Morokuma[73] (see Tables S2 and S3).

Analyzing the bond length distances along the retinal conjugated chain (Figure 10 and Table S2), we found that the **bR-O1**/TiO_2, **bR-O2**/TiO_2, **bR-O3**/TiO_2, and **bR-O4**/TiO_2 show an average deviation of bond-length distances of 0.019, 0.015, 0.018, and 0.013 Å compared to that of isolated bR. Additionally, we analyzed the BLA, which was calculated as the difference between the average single bond lengths and double bond lengths in the retinal chain.[83,84] The BLA value gets closer to 0 as the structure becomes bond delocalized. In our case, the retinal of the isolated bR has a BLA value of 0.033, while the BLA values of the bR/TiO_2 systems show an increased bond-length alternation (0.071, 0.064, 0.070, and 0.058 for the retinal of **bR-O1**/TiO_2, **bR-O2**/TiO_2, **bR-O3**/TiO_2, and **bR-O4**/TiO_2).

Moreover, we analyzed the partial charge distributions along the retinal conjugated chain (Figure 11 and Table S3). In

https://doi.org/10.1021/acs.jctc.4c01370
J. Chem. Theory Comput. 2025, 21, 3231−3245

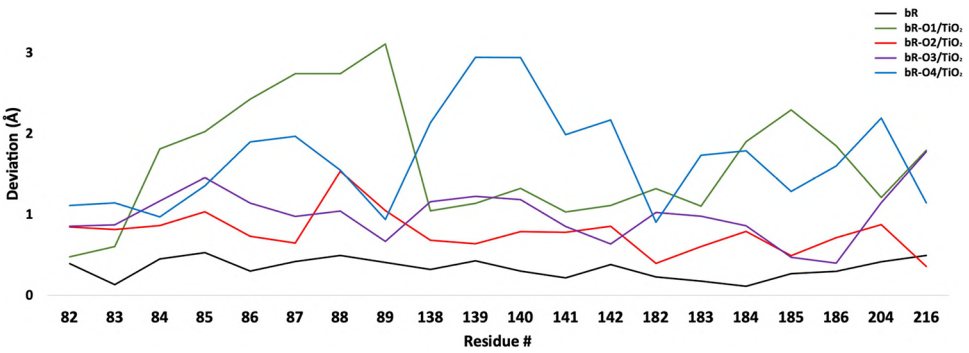

Figure 9. Deviations of C−α coordinates of the amino acids present in the cavity of the optimized isolated bR and **bR-O1**/TiO_2, **bR-O2**/TiO_2, **bR-O3**/TiO_2, and **bR-O4**/TiO_2 systems with respect to the bR crystallographic structure.

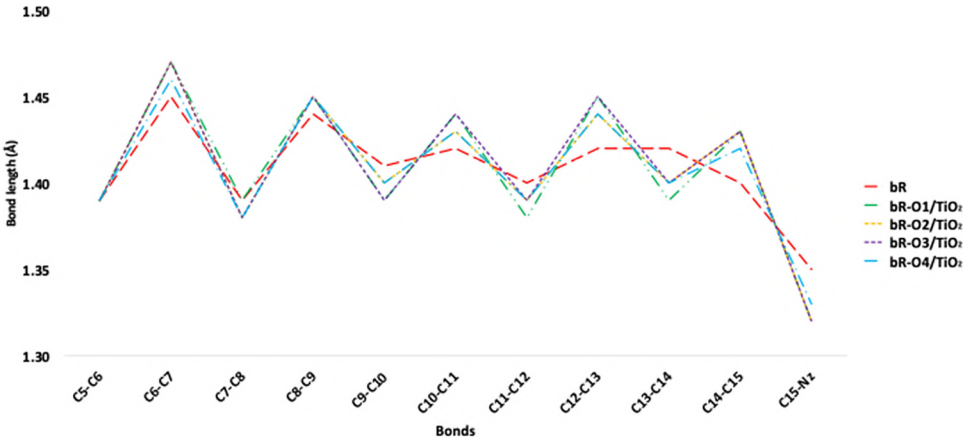

Figure 10. Bond lengths distances (Å) along the retinal conjugated chain of **bR-O1**/TiO_2, **bR-O2**/TiO_2, **bR-O3**/TiO_2, **bR-O4**/TiO_2 in comparison to those of retinal in the isolated bR model.

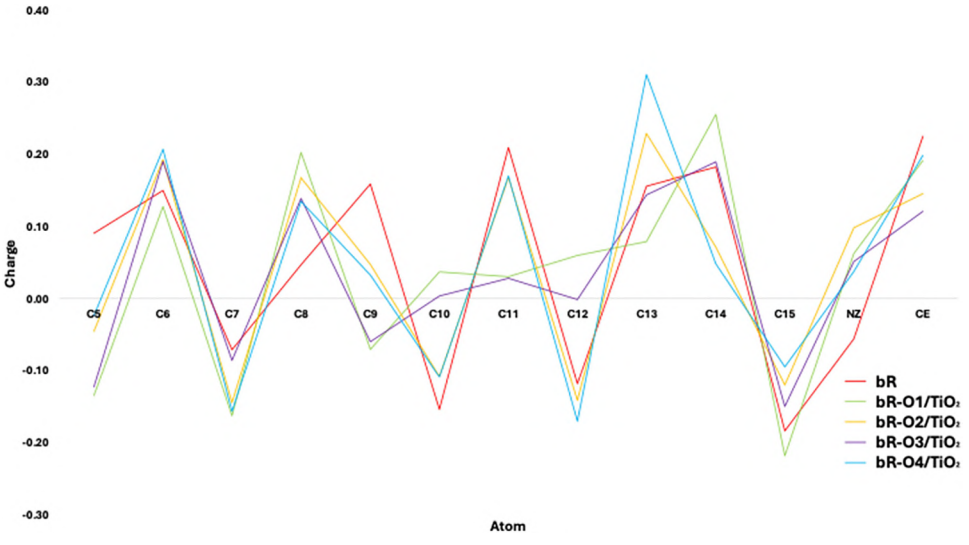

Figure 11. Mulliken partial charge distribution along the retinal conjugated chain (including C_5−C_{15}, N_Z and C_ε QM atoms) of **bR-O1**/TiO_2, **bR-O2**/TiO_2, **bR-O3**/TiO_2, and **bR-O4**/TiO_2 in comparison to that of the retinal in the isolated bR model. Hydrogen partial charges are added into the partial charge of their respective linked carbons or nitrogen atoms. The total Mulliken partial charge distribution is equal to one adding the contribution of the remaining QM atoms.

particular, following the work of Palombo et al.,[84] we calculated the summation of the partial charges residing on the C_{14}−C_ε moiety (from now on, it will be called $Charge_{PSB}$). The higher the value of the $Charge_{PSB}$, the more localized the positive charge is on the C_{14}−C_ε moiety.[84] As for the BLA values, the $Charge_{PSB}$ of bR/TiO_2 systems shows a more localized charge on the C_{14}−C_ε moiety (0.63, 0.27, 0.34, and 0.31 for **bR-O1**/TiO_2, **bR-O2**/TiO_2, **bR-O3**/TiO_2, and **bR-O4**/TiO_2) compared to that of the isolated bR (0.19). Hence, we can observe that the BLA and $Charge_{PSB}$ values exhibit the

https://doi.org/10.1021/acs.jctc.4c01370
J. Chem. Theory Comput. 2025, 21, 3231−3245

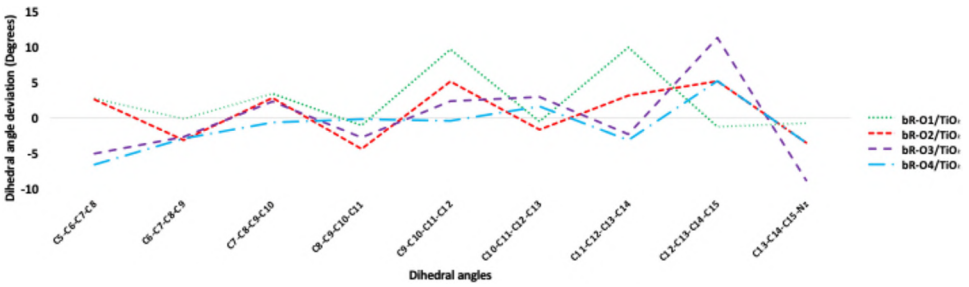

Figure 12. Dihedral angles deviation (°) along the retinal conjugated chain of **bR-O1**/TiO_2, **bR-O2**/TiO_2, **bR-O3**/TiO_2, and **bR-O4**/TiO_2 with respect to the isolated bR model optimized in this work.

Table 5. TD-DFT Absorption Maxima (λ^a_{max}), Vertical Excitation Energies (E_{exc}), Oscillator Strengths (f), and Orbital Transition Contributions (%) to the Excitations of bR-O1/TiO_2, bR-O2/TiO_2, bR-O3/TiO_2, and bR-O4/TiO_2 Systems at the CAM-B3LYP/6-31+G(d) ([a]) and M06-2X/6-31+G(d) ([b]) Levels of Theory[c]

	λ^a_{max} (nm)		E_{exc} (eV)		f		contrib. (%)	
	a	*b*	*a*	*b*	*a*	*b*	*a*	*b*
bR	566	577	2.19	2.15	1.5	1.5	96% H → L	98% H → L
bR-O1/TiO_2	478	485	2.59(0.40)	2.56(0.41)	1.4	1.3	95% H → L	96% H → L
bR-O2/TiO_2	522	532	2.38(0.19)	2.33(0.18)	1.5	1.4	95% H → L	97% H → L
bR-O3/TiO_2	485	492	2.56(0.37)	2.52(0.37)	1.4	1.4	95% H → L	96% H → L
bR-O4/TiO_2	534	544	2.32(0.13)	2.28(0.13)	1.4	1.3	96% H → L	97% H → L

[a]Calculations performed at CAM-B3LYP/6-31+G(d) level of theory. [b]Calculations performed at M06-2X/6-31+G(d) level of theory. [c]The energy differences (eV) between the computed absorption maxima of bR/TiO_2 systems and those of isolated bR optimized in this work are shown in parentheses.

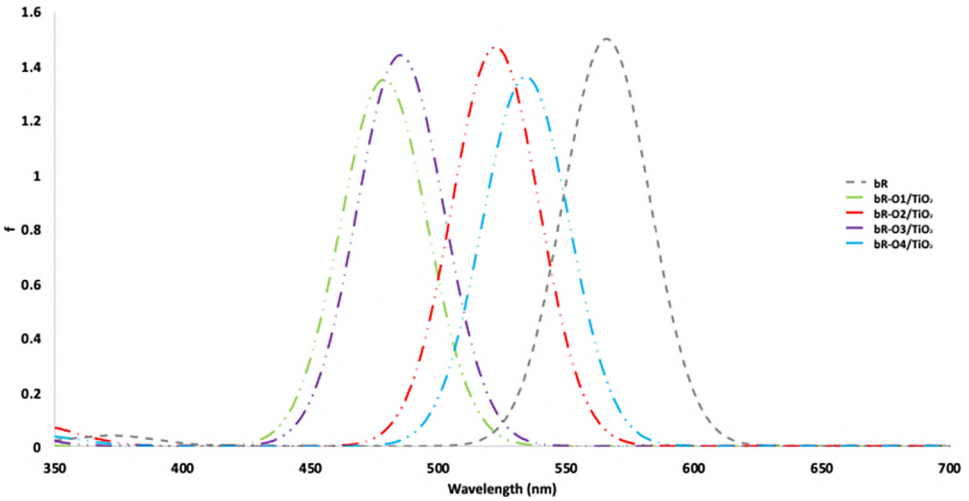

Figure 13. CAM-B3LYP/6-31+G(d) plotted UV−Vis spectra of isolated bR, **bR-O1**/TiO_2, **bR-O2**/TiO_2, **bR-O3**/TiO_2, and **bR-O4**/TiO_2 using Molden 5.6 and a Gaussian distribution (half bandwidth set to 20 nm).[76]

same trend. This is expected when considering a simple Lewis resonance formula interpretation of the positive charge delocalization. In fact, this involves an increased weight of the resonance formula with an inverted bond order (a charge transfer formula) with respect to the usual Lewis formula for a ground-state retinal chromophore.

Focusing attention on dihedral angles, none of the bR/TiO_2 hybrid systems present significant deviations from the dihedral angles' values of the isolated bR (Figure 12 and Table S4). Indeed, the average deviations were calculated as 3.26, 3.49, 4.49, and 2.66°, respectively, for **bR-O1**/TiO_2, **bR-O2**/TiO_2, **bR-O3**/TiO_2, and **bR-O4**/TiO_2. Moreover, we can affirm that all the analyzed systems show bond lengths and dihedral angle values in good agreement with those calculated using the ONIOM(B3LYP:Amber)-EE methodology in the work of Vreven & Morokuma[73] (Tables S2 and S3). The results of all these analyses let us assume that the retinal geometries of **bR-O1**/TiO_2, **bR-O2**/TiO_2, **bR-O3**/TiO_2, and **bR-O4**/TiO_2 are adequately preserved after the adsorption process. Furthermore, previous findings in the literature reported that a lower delocalization of the positive charge along the polyene chain and higher BLA values correspond to blue-shifted absorption values.[89] Consistently, we can expect that all of the hybrid systems will exhibit blue-shifted absorption maxima compared to that of the isolated bR.

3.4. UV−Vis Vertical Excitation Properties of bR-O1/TiO_2, bR-O2/TiO_2, bR-O3/TiO_2, and bR-O4/TiO_2 Systems.

To investigate the possible differences in the UV−Vis

https://doi.org/10.1021/acs.jctc.4c01370
J. Chem. Theory Comput. 2025, 21, 3231−3245

absorption maxima of isolated bR and bR/TiO_2 systems, the excitation energies of **bR-O1**/TiO_2, **bR-O2**/TiO_2, **bR-O3**/TiO_2, and **bR-O4**/TiO_2 were calculated at the CAM-B3LYP/6-31+G(d) and M06-2*X*/6-31+G(d) levels of theory by using the ONIOM-EE methodology. Absorption maxima (λ^{a}_{max}), vertical excitation energies (E_{exc}), oscillator strengths (f), and composition (%) in terms of molecular orbitals to the transitions are reported in Table 5. The plotted UV−Vis spectra at the CAM-B3LYP/6-31+G(d) level of theory are reported in Figure 13. Experimentally, two protocols were reported to adsorb the bR on TiO_2.[26] The first one regards the physisorption of bR on the TiO_2 surface, which results in a broad absorption peak at ca. 530 nm (2.34 eV) with respect to that of native bR at 568 nm (2.18 eV). The other protocol includes the use of the 3-mercaptopropionic acid as a linker to immobilize the bR to the TiO_2 surface, a commonly employed technique to immobilize proteins,[56,85] and it results in a definite peak at ca. 560 nm (2.21 eV). In both cases, the sensitization of bR on TiO_2 leads to a shift toward the blue region of the spectrum, although for the chemically linked bR the shift is smaller.[26]

Since the bR/TiO_2 hybrid systems developed in this work were simulated according to a physisorption mechanism, we could expect absorption maxima values similar to those experimentally registered following the physisorption protocol.

We calculated absorption maxima in the range of 478−534 nm (2.59−2.32 eV) at the CAM-B3LYP/6-31+G(d) level and 485−544 nm (2.56−2.28 eV) at the M06-2*X*/6-31+G(d) level for **bR-O1**/TiO_2, **bR-O2**/TiO_2, **bR-O3**/TiO_2, and **bR-O4**/TiO_2 (Table 5). In agreement with experimental findings, these values are all blue-shifted when compared to the computed value (2.19 eV at CAM-B3LYP/6-31+G(d) and 2.15 eV M06-2*X*/6-31+G(d) levels) of the isolated bR (see Table 5 and Figure 13). These blue-shifted values reflect the lower delocalization of the positive charge through the polyene chain and higher BLA values[86] of the hybrid systems compared to those of the isolated bR.

To gain further insights into the excited state properties of bR, we also investigated the possible influence of the protein environment on the chromophore spectroscopic properties. Indeed, the bare chromophore was extracted from the optimized QM/MM bR structure, and its excitation energy was calculated at the M06-2*X*/6-31+G(d) level of theory in the gas phase. Related data at the CAM-B3LYP/6-31+G(d) level of theory are shown in Table S5. We calculated an intense (f = 2.1) absorption maximum at 539 nm (2.30 eV), which is associated with a $\pi \rightarrow \pi^*$ transition that involves HOMO → LUMO orbitals. Hence, the interaction between the chromophore and the protein environment accounts for 0.07 eV toward the blue region, which is part of the opsin shift, i.e., the protein-induced spectral shift of the retinal absorption,[87−89] in good agreement with literature data.[73,90]

4. CONCLUSIONS

In this work, we reported an *in silico* study of a gas-phase, isolated bR/TiO_2 system based on SMD-MD and QM/MM simulations which were applied to investigate four different bR orientations on the anatase TiO_2 surface. While a realistic model of the bR/TiO_2 hybrid system would be extremely complex and computationally expensive, here we assumed that the initial contact of bR with the TiO_2 surface would not change the characteristics of the "unperturbed" protein. Indeed, the developed bR/TiO_2 models successfully allowed us to unveil the principal protein−surface interactions and to describe the change in the spectral properties of bR when it gets in contact with the surface. In particular, our results showed that the electrostatic interactions are the principal component of the adsorption mechanism, and in agreement with experimental findings, we found a blue shift in the absorption maximum value when the bR is adsorbed on TiO_2 that validates the TiO_2-induced geometrical and electronic modifications of the chromophore moiety revealed using our models. These outcomes could be particularly useful in classifying or disentangling the "single" effects that characterize a more complex interaction or those measured in real systems. Based on these results, we propose that constructed models for the bR/TiO_2 hybrid system could be employed in future studies focusing on the electron transfer mechanism in bR-based solar energy conversion devices, currently pursued in our laboratories. Indeed, taking advantage of methodological development available in the literature (see refs 91−96), and when it applies, the quantum mechanical description of the electronic structure of the TiO_2 surface, the understanding of the active sites that facilitate long-range electron transfer from the retinal chromophore (donor) to the TiO_2 surface (acceptor) will hold significant implications for solar energy applications. It is hoped that the outcome of these studies would provide the information necessary for improving the overall photocurrent efficiency of such devices (e.g., lead to novel bR mutants with enhanced electron transfer properties).

■ ASSOCIATED CONTENT

Supporting Information

The Supporting Information is available free of charge at https://pubs.acs.org/doi/10.1021/acs.jctc.4c01370.

Point charges at the frontier atoms, interaction energies along SMD/MD simulations, bond length, partial charges and dihedral angle of the PRSB, and vertical excitation energies of the bare chromophore (PDF)

■ AUTHOR INFORMATION

Corresponding Author

Adalgisa Sinicropi − *R2ES Lab, Department of Biotechnology, Chemistry and Pharmacy, University of Siena, 53100 Siena, Italy; Italian National Council for Research - Institute for the Chemistry of OrganoMetallic Compounds (CNR-ICCOM), 50019 Sesto Fiorentino, Italy; CSGI, Consorzio per lo Sviluppo dei Sistemi a Grande Interfase, 50019 Sesto Fiorentino, Italy;* orcid.org/0000-0001-5605-6482; Email: adalgisa.sinicropi@unisi.it

Authors

Mayra Avelar − *R2ES Lab, Department of Biotechnology, Chemistry and Pharmacy, University of Siena, 53100 Siena, Italy*

Carmen Coppola − *R2ES Lab, Department of Biotechnology, Chemistry and Pharmacy, University of Siena, 53100 Siena, Italy; Italian National Council for Research - Institute for the Chemistry of OrganoMetallic Compounds (CNR-ICCOM), 50019 Sesto Fiorentino, Italy; CSGI, Consorzio per lo Sviluppo dei Sistemi a Grande Interfase, 50019 Sesto Fiorentino, Italy;* orcid.org/0000-0002-8050-7615

Alessio d'Ettorre − *R2ES Lab, Department of Biotechnology, Chemistry and Pharmacy, University of Siena, 53100 Siena, Italy*

https://doi.org/10.1021/acs.jctc.4c01370
J. Chem. Theory Comput. 2025, 21, 3231−3245

Andrea Ienco − *Italian National Council for Research - Institute for the Chemistry of OrganoMetallic Compounds (CNR-ICCOM), 50019 Sesto Fiorentino, Italy;* orcid.org/0000-0002-2586-4943

Maria Laura Parisi − *R2ES Lab, Department of Biotechnology, Chemistry and Pharmacy, University of Siena, 53100 Siena, Italy; Italian National Council for Research - Institute for the Chemistry of OrganoMetallic Compounds (CNR-ICCOM), 50019 Sesto Fiorentino, Italy; CSGI, Consorzio per lo Sviluppo dei Sistemi a Grande Interfase, 50019 Sesto Fiorentino, Italy*

Riccardo Basosi − *R2ES Lab, Department of Biotechnology, Chemistry and Pharmacy, University of Siena, 53100 Siena, Italy; Italian National Council for Research - Institute for the Chemistry of OrganoMetallic Compounds (CNR-ICCOM), 50019 Sesto Fiorentino, Italy; CSGI, Consorzio per lo Sviluppo dei Sistemi a Grande Interfase, 50019 Sesto Fiorentino, Italy*

Annalisa Santucci − *Department of Biotechnology, Chemistry and Pharmacy, University of Siena, 53100 Siena, Italy;* orcid.org/0000-0001-6976-9086

Massimo Olivucci − *Department of Biotechnology, Chemistry and Pharmacy, University of Siena, 53100 Siena, Italy; Department of Chemistry and Center for Photochemical Sciences, Bowling Green State University, Bowling Green, Ohio 43403, United States*

Complete contact information is available at: https://pubs.acs.org/10.1021/acs.jctc.4c01370

Author Contributions

#M.A. and A.E. contributed equally.

Notes

The authors declare no competing financial interest.

■ ACKNOWLEDGMENTS

Authors acknowledge the Department of Biotechnology, Chemistry, and Pharmacy, Department of Excellence 2018-2022, and the hpc@dbcf for providing computational resources. The computing resources and the related technical support have also been provided by CRESCO/ENEAGRID High Performance Computing infrastructure and its staff.[97] CRESCO/ENEAGRID High Performance Computing infrastructure is funded by ENEA, the Italian National Agency for New Technologies, Energy and Sustainable Economic Development, and by Italian and European research programs, see http://www.cresco.enea.it/english for information.

■ REFERENCES

(1) Oesterhelt, D.; Stoeckenius, W. Functions of a New Photoreceptor Membrane. *Proc. Natl. Acad. Sci. U.S.A.* **1973**, *70* (10), 2853−2857.

(2) Oesterhelt, D.; Stoeckenius, W. Isolation of the Cell Membrane of Halobacterium Halobium and Its Fractionation into Red and Purple Membrane. *Methods Enzymol* **1974**, *31*, 667−678.

(3) Lozier, R. H.; Bogomolni, R. A.; Stoeckenius, W. Bacteriorhodopsin: A Light-Driven Proton Pump in Halobacterium Halobium. *Biophys. J.* **1975**, *15* (9), 955−962.

(4) Khorana, G. H.; Gerber, G. E.; Herlihy, W. C.; Gray, C. P.; Anderegg, R.; Nihei, K.; Biemann, K. Amino Acid Sequence of Bacteriorhodopsin. *Proc. Natl. Acad. Sci. U. S. A.* **1979**, *76* (10), 5046−5050.

(5) Ovchinnikov, Y. A.; Abdulaev, N. G.; Feigina, M. Y.; Kiselev, A. V.; Lobanov, A. The Structural Basis of the Functioning of Bacteriorhodopsin: An Overview. *Elsevier/North-Holland Biomedical Pres* **1979**, *100* (2), 219−224.

(6) Engelman, D. M.; Henderson, R.; Mclachlan, A. D. Path of the Polypeptide in Bacteriorhodopsin. *Proc. Natl. Acad. Sci. U. S. A.* **1980**, *77* (4), 2023−2027.

(7) Luecke, H.; Schobert, B.; Richter, H.; Cartailler, J.; Lanyi, J. K. Structure of Bacteriorhodopsin at 1.55 Å Resolution. *J. Mol. Biol.* **1999**, *291*, 899−911.

(8) Mathies, R. A. From Femtoseconds to Biology: Mechanism of Bacteriorhodopsin's Light-Driven Proton Pump. *Proc. Indian Acad. Sci. (Chem. Sci.)* **1991**, *103* (3), 283−293.

(9) Lanyi, J. K. Bacteriorhodopsin. *Annu. Rev. Physiol.* **2004**, *66*, 665−688.

(10) Nogly, P.; Weinert, T.; James, D.; Carbajo, S.; Ozerov, D.; Furrer, A.; Gashi, D.; Borin, V.; Skopintsev, P.; Jaeger, K.; Nass, K.; Båth, P.; Bosman, R.; Koglin, J.; Seaberg, M.; Lane, T.; Kekilli, D.; Brünle, S.; Tanaka, T.; Wu, W.; Milne, C.; White, T.; Barty, A.; Weierstall, U.; Panneels, V.; Nango, E.; Iwata, S.; Hunter, M.; Schapiro, I.; Schertler, G.; Neutze, R.; Standfuss, J. Retinal Isomerization in Bacteriorhodopsin Captured by a Femtosecond X-Ray Laser. *Science* **2018**, *361* (6398), No. eaat0094.

(11) Kovacs, G. N.; Colletier, J. P.; Grünbein, M. L.; Yang, Y.; Stensitzki, T.; Batyuk, A.; Carbajo, S.; Doak, R. B.; Ehrenberg, D.; Foucar, L.; Gasper, R.; Gorel, A.; Hilpert, M.; Kloos, M.; Koglin, J. E.; Reinstein, J.; Roome, C. M.; Schlesinger, R.; Seaberg, M.; Shoeman, R. L.; Stricker, M.; Boutet, S.; Haacke, S.; Heberle, J.; Heyne, K.; Domratcheva, T.; Barends, T. R. M.; Schlichting, I. Three-Dimensional View of Ultrafast Dynamics in Photoexcited Bacteriorhodopsin. *Nat. Commun.* **2019**, *10*, 3177.

(12) Shen, Y.; Safinyia, C. R.; Liang, K. S.; Ruppert, A. F.; Rothschild, K. J. Stabilization of the Membrane Protein Bacteriorhodopsin to 140 °C in Two-Dimensional Films. *Nature* **1993**, *366*, 48−50.

(13) Cladera, J.; Galisteo, M. L.; Sabes, M.; Mateo, P. L.; Padrós, E. The Role of Retinal in the Thermal Stability of the Purple Membrane. *Eur. J. Biochem.* **1992**, *207*, 581−585.

(14) Hampp, N. Bacteriorhodopsin as a Photochromic Retinal Protein for Optical Memories. *Chem. Rev.* **2000**, *100*, 1755−1776.

(15) Wang, J.; Link, S.; Heyes, C. D.; El-sayed, M. A. Comparison of the Dynamics of the Primary Events of Bacteriorhodopsin in Its Trimeric and Monomeric States. *Biophys. J.* **2002**, *83* (3), 1557−1566.

(16) Hamm, P.; Zurek, M.; Röschinger, T.; Patzelt, H.; Oesterhelt, D.; Zinth, W. Femtosecond Spectroscopy of the Photoisomerisation of the Protonated Schiff Base of All-Trans Retinal. *Chem. Phys. Lett.* **1996**, *263*, 613−621.

(17) Li, Y. T.; Tian, Y.; Tian, H.; Tu, T.; Gou, G. Y.; Wang, Q. A Review on Bacteriorhodopsin-Based Bioelectronic Devices. *Sensors* **2018**, *18*, 1368.

(18) Wagner, N. L.; Greco, J. A.; Ranaghan, M. J.; Birge, R. R. Directed Evolution of Bacteriorhodopsin for Applications in Bioelectronics. *J. R Soc. Interface* **2013**, *10* (84), 20130197.

(19) Lv, Y.; Liang, D.; Lu, S.; Aurbach, D.; Xiang, Y. Unidirectional Electron Injection and Accelerated Proton Transport in Bacteriorhodopsin Based Bio-p-n Junctions. *Biosens Bioelectron* **2021**, *173*, No. 112811.

(20) Ashwini, R.; Vijayanand, S.; Hemapriya, J. Photonic Potential of Haloarchaeal Pigment Bacteriorhodopsin for Future Electronics: A Review. *Curr. Microbiol.* **2017**, *74*, 996−1002.

(21) Singh, P.; Singh, S.; Jaggi, N.; Kim, K.; Devi, P. Recent Advances in Bacteriorhodopsin-Based Energy Harvesters and Sensing Devices. *Nano Energy* **2021**, *79*, No. 105482.

(22) Lin, J.; Li, X. R.; Zhao, L. Y.; Li, G. P.; Shen, H. Y.; Li, Y. T.; Ren, T. L. Review on Bacteriorhodopsin-Based Self-Powered Bio-Photoelectric Sensors. *Mater. Sci. Semicond. Process* **2023**, *162*, No. 107501.

(23) Patel, R.; Salamone, G.; Macwan, I. The Role of Graphene Monolayers in Enhancing the Yield of Bacteriorhodopsin Photostates for Optical Memory Applications. *Applied Sciences* **2021**, *11*, 9698.

(24) Balasubramanian, S.; Wang, P.; Schaller, R. D.; Rajh, T.; Rozhkova, E. A. High-Performance Bioassisted Nanophotocatalyst for Hydrogen Production. *Nano Lett.* **2013**, *13* (7), 3365−3371.
(25) Naseri, N.; Jafanza, S.; Irani, R. Visible-Switchable BR/TiO_2 Nanostructured Photoanodes for Bio-Inspired Solar Energy Conversion. *RSC Adv.* **2015**, *5*, 18642−18646.
(26) Allam, N. K.; Yen, C.-W.; Near, R. D.; El-Sayed, M. A. Bacteriorhodopsin/TiO_2 Nanotube Arrays Hybrid System for Enhanced Photoelectrochemical Water Splitting. *Energy Environ. Sci.* **2011**, *4* (8), 2909−2914.
(27) Johnson, K. E.; Gakhar, S.; Risbud, S. H.; Longo, M. L. Development and Characterization of Titanium Dioxide Gel with Encapsulated Bacteriorhodopsin for Hydrogen Production. *Langmuir* **2018**, *34* (25), 7488−7496.
(28) Dai, G.; Chao, L. M.; Iwasa, T. Photocatalytic Degradation of Phenol with Bacteriorhodopsin Sensitized TiO_2 Nanoparticles. *Adv. Mat Res.* **2014**, *955−959*, 415−418.
(29) Keshavarz, E.; Molaeirad, A. Application of Flexible Sheet in the Construction of Bio-Battery through Using Immobilized Bacteriorhodopsin. *Arch. Biol. Sci.* **2019**, *102*.
(30) Mohammadpour, R.; Janfaza, S. Efficient Nanostructured Biophotovoltaic Cell Based on Bacteriorhodopsin as Biophotosensitizer. *ACS Sustain Chem. Eng.* **2015**, *3* (5), 809−813.
(31) Mohammadpour, R.; Janfaza, S.; Zeinoddini, M. Potential of Light-Harvesting of Bacteriorhodopsin Co-Sensitized with Green Fluorescence Protein: A New Insight into Bioenergy Application. *Biomass Bioenergy* **2016**, *87*, 35−38.
(32) Das, S.; Wu, C.; Song, Z.; Hou, Y.; Koch, R.; Somasundaran, P.; Priya, S.; Barbiellini, B.; Venkatesan, R. Bacteriorhodopsin Enhances Efficiency of Perovskite Solar Cells. *ACS Appl. Mater. Interfaces* **2019**, *11*, 30728−30734.
(33) Jeganathan, C.; Sabari Girisun, T. C.; Vijaya, S.; Anandan, S. Bacteriorhodopsin-Sensitized Preferentially Oriented One-Dimensional TiO_2 Nanorod Polymorphs as Efficient Photoanodes for High-Performance Bio-Sensitized Solar Cells. *Appl. Nanosci* **2019**, *9* (2), 189−208.
(34) Jeganathan, C.; Girisun, T. C. S.; Vijaya, S.; Anandan, S. Improved Charge Collection and Photo Conversion of Bacteriorhodopsin Sensitized Solar Cells Coupled with Reduced Graphene Oxide Decorated One-Dimensional TiO_2 Nanorod Hybrid Photoanodes. *Electrochim. Acta* **2019**, *319*, 909−921.
(35) Girisun Sabari, T. C.; Jeganathan, C.; Pavithra, N.; Anandan, S. Structurally Modified Bacteriorhodopsin as an Efficient Bio-Sensitizer for Solar Cell Applications. *Eur. Biophys. J.* **2019**, *48*, 61−71.
(36) Duquet, F.; Nada, A. A.; Rivallin, M.; Rouessac, F.; Villeneuve-faure, C.; Roualdes, S. Influence of Bio-Based Surfactants on TiO_2 Thin Films as Photoanodes for Electro-Photocatalysis. *Catalysts* **2021**, *11* (10), 1228.
(37) Mahyad, B.; Janfaza, S.; Sadat, E. Bio-Nano Hybrid Materials Based on Bacteriorhodopsin: Potential Applications and Future Strategies. *Adv. Colloid Interface Sci.* **2015**, *225*, 194−202.
(38) Thavasi, V.; Lazarova, T.; Filipek, S.; Kolinski, M.; Querol, E.; Kumar, A.; Ramakrishna, S.; Padrós, E.; Renugopalakrishnan, V. Study on the Feasibility of Bacteriorhodopsin as Bio-Photosensitizer in Excitonic Solar Cell: A First Report. *J. Nanosci. Nanotechnol.* **2009**, *9* (3), 1679−1687.
(39) Chellamuthu, J.; Nagaraj, P.; Girisun, S.; Sambandam, A.; Muthupandian, A. Enhanced Photocurrent Generation in Bacteriorhodopsin Based Bio-Sensitized Solar Cells Using Gel Electrolyte. *J. Photochem. Photobiol. B* **2016**, *162*, 208−212.
(40) Molaeirad, A.; Janfaza, S.; Karimi-fard, A.; Mahyad, B. Photocurrent Generation by Adsorption of Two Main Pigments of Halobacterium Salinarum on TiO_2 Nanostructured Electrode. *Biotechnol Appl. Biochem* **2015**, *62*, 121−125.
(41) Janfaza, S.; Molaeirad, A.; Mohammadpour, R.; Khayati, M.; Mehrvand, J. Efficient Bio-Nano Hybrid Solar Cells via Purple Membrane as Sensitizer. *BioNanoSci.* **2014**, *4*, 71−77.
(42) Wang, P.; Dimitrijevic, N. M.; Chang, A. Y.; Schaller, R. D.; Liu, Y.; Rajh, T.; Rozhkova, E. A. Photoinduced Electron Transfer Pathways in Hydrogen-Evolving Reduced Graphene Oxide-Boosted Hybrid Nano-Bio Catalyst. *ACS Nano* **2014**, *8* (8), 7995−8002.
(43) Pedraza-González, L.; De Vico, L.; Marín, M. D. C.; Fanelli, F.; Olivucci, M. A-ARM: Automatic Rhodopsin Modeling with Chromophore Cavity Generation, Ionization State Selection, and External Counterion Placement. *J. Chem. Theory Comput* **2019**, *15* (5), 3134−3152.
(44) Kühne, T. D.; Iannuzzi, M.; Del Ben, M.; Rybkin, V. V.; Seewald, P.; Stein, F.; Laino, T.; Khaliullin, R. Z.; Schütt, O.; Schiffmann, F.; Golze, D.; Wilhelm, J.; Chulkov, S.; Bani-Hashemian, M. H.; Weber, V.; Borštnik, U.; Taillefumier, M.; Jakobovits, A. S.; Lazzaro, A.; Pabst, H.; Müller, T.; Schade, R.; Guidon, M.; Andermatt, S.; Holmberg, N.; Schenter, G. K.; Hehn, A.; Bussy, A.; Belleflamme, F.; Tabacchi, G.; Glöß, A.; Lass, M.; Bethune, I.; Mundy, C. J.; Plessl, C.; Watkins, M.; VandeVondele, J.; Krack, M.; Hutter, J. CP2K: An Electronic Structure and Molecular Dynamics Software Package -Quickstep: Efficient and Accurate Electronic Structure Calculations. *J. Chem. Phys.* **2020**, *152*, 194103.
(45) Ferré, N.; Olivucci, M. Probing the Rhodopsin Cavity with Reduced Retinal Models at the CASPT2//CASSCF/AMBER Level of Theory. *J. Am. Chem. Soc.* **2003**, *125* (23), 6868−6869.
(46) Perdew, J. P.; Burke, K.; Ernzerhof, M. Generalized Gradient Approximation Made Simple. *Phys. Rev. Lett.* **1996**, *77* (18), 3865−3868.
(47) Huang, J.; Mackerell, A. D. CHARMM36 All-Atom Additive Protein Force Field: Validation Based on Comparison to NMR Data. *J. Comput. Chem.* **2013**, *34* (25), 2135−2145.
(48) Vandevondele, J.; Krack, M.; Mohamed, F.; Parrinello, M.; Chassaing, T.; Hutter, J. Quickstep: Fast and Accurate Density Functional Calculations Using a Mixed Gaussian and Plane Waves Approach. *Comput. Phys. Commun.* **2005**, *167* (2), 103−128.
(49) Maseras, F.; Morokuma, K. IMOMM: A New Integrated Ab Initio + Molecular Mechanics Geometry Optimization Scheme of Equilibrium Structures and Transition States. *J. Comput. Chem.* **1995**, *16* (9), 1170−1179.
(50) Gao, J.; Amara, P.; Alhambra, C.; Field, M. J. A Generalized Hybrid Orbital (GHO) Method for the Treatment of Boundary Atoms in Combined QM/MM Calculations. *J. Phys. Chem. A* **1998**, *102* (24), 4714−4721.
(51) Krack, M. Pseudopotentials for H to Kr Optimized for Gradient-Corrected Exchange-Correlation Functionals. *Theor. Chem. Acc.* **2005**, *114*, 145−152.
(52) Luttrell, T.; Halpegamage, S.; Tao, J.; Kramer, A.; Sutter, E.; Batzill, M. Why Is Anatase a Better Photocatalyst than Rutile? - Model Studies on Epitaxial TiO_2 Films. *Sci. Rep* **2014**, *4* (4043), 1−8.
(53) Zhang, J.; Zhou, P.; Liu, J.; Yu, J. New Understanding of the Difference of Photocatalytic Activity among Anatase, Rutile and Brookite TiO_2. *Phys. Chem. Chem. Phys.* **2014**, *16*, 20382−20386.
(54) Katal, R.; Masudy-Panah, S.; Tanhaei, M.; Farahani, M. H. D. A.; Jiangyong, H. A Review on the Synthesis of the Various Types of Anatase TiO_2 Facets and Their Applications for Photocatalysis. *J. Chem. Eng.* **2020**, *384*, No. 123384.
(55) Koch, R.; Lipton, A. S.; Filipek, S.; Renugopalakrishnan, V. Arginine Interactions with Anatase TiO_2 (100) Surface and the Perturbation of ^{49}Ti NMR Chemical Shifts - A DFT Investigation: Relevance to Renu-Seeram Bio Solar Cell. *J. Mol. Model* **2011**, *17* (6), 1467−1472.
(56) Shervedani, R. K.; Hemmatian, Z.; Hatefi-Mehrjardi, A. Immobilization of L-Lysine α-Oxidase on Gold-Mercaptopropionic Acid Self-Assembled Monolayer: Preparation and Electrochemical Characterization. *Bioelectrochemistry* **2009**, *75* (2), 124−129.
(57) *Schrödinger Release 2022−3. Maestro*; Schrödinger, LLC: New York, NY. 2021.
(58) Phillips, J. C.; Braun, R.; Wang, W.; Gumbart, J.; Tajkhorshid, E.; Villa, E.; Chipot, C.; Skeel, R. D.; Kalé, L.; Schulten, K. Scalable Molecular Dynamics with NAMD. *J. Comput. Chem.* **2005**, *26* (16), 1781−1802.
(59) Best, R. B.; Zhu, X.; Shim, J.; Lopes, P. E. M.; Mittal, J.; Feig, M.; MacKerell, A. D. Optimization of the Additive CHARMM All-

https://doi.org/10.1021/acs.jctc.4c01370
J. Chem. Theory Comput. 2025, 21, 3231−3245

Atom Protein Force Field Targeting Improved Sampling of the Backbone φ, ψ and Side-Chain X_1 and X_2 Dihedral Angles. *J. Chem. Theory Comput* **2012**, *8* (9), 3257−3273.
(60) MacKerell, A. D.; Bashford, D.; Bellott, M.; Dunbrack, R. L.; Evanseck, J. D.; Field, M. J.; Fischer, S.; Gao, J.; Guo, H.; Ha, S.; Joseph-McCarthy, D.; Kuchnir, L.; Kuczera, K.; Lau, F. T. K.; Mattos, C.; Michnick, S.; Ngo, T.; Nguyen, D. T.; Prodhom, B.; Reiher, W. E.; Roux, B.; Schlenkrich, M.; Smith, J. C.; Stote, R.; Straub, J.; Watanabe, M.; Wiórkiewicz-Kuczera, J.; Yin, D.; Karplus, M. All-Atom Empirical Potential for Molecular Modeling and Dynamics Studies of Proteins. *J. Phys. Chem. B* **1998**, *102* (18), 3586−3616.
(61) MacKerell, A. D.; Feig, M.; Brooks, C. L. Improved Treatment of the Protein Backbone in Empirical Force Fields. *J. Am. Chem. Soc.* **2004**, *126* (3), 698−699.
(62) Utesch, T.; Daminelli, G.; Mroginski, M. A. Molecular Dynamics Simulations of the Adsorption of Bone Morphogenetic Protein-2 on Surfaces with Medical Relevance. *Langmuir* **2011**, *27* (21), 13144−13153.
(63) Mücksch, C.; Urbassek, H. M. Forced Desorption of Bovine Serum Albumin and Lysozyme from Graphite: Insights from Molecular Dynamics Simulation. *J. Phys. Chem. B* **2016**, *120* (32), 7889−7895.
(64) Mücksch, C.; Urbassek, H. M. Accelerating Steered Molecular Dynamics: Toward Smaller Velocities in Forced Unfolding Simulations. *J. Chem. Theory Comput* **2016**, *12* (3), 1380−1384.
(65) Brandt, E. G.; Lyubartsev, A. P. Systematic Optimization of a Force Field for Classical Simulations of TiO_2-Water Interfaces. *J. Phys. Chem. C* **2015**, *119* (32), 18110−18125.
(66) Humphrey, W.; Dalke, A.; Schulten, K. VMD: Visual Molecular Dynamics. *J. Mol. Graph* **1996**, *14*, 33−38.
(67) Frisch, M. J.; Trucks, G. W.; Schlegel, H. B.; Scuseria, G. E.; Robb, M. A.; Cheeseman, J. R.; Scalmani, G.; Barone, V.; Petersson, G. A.; Nakatsuji, H.; Li, X.; Caricato, M.; Marenich, A. V.; Bloino, J.; Janesko, B. G.; Gomperts, R.; Mennucci, B.; Hratchian, H. P.; Ortiz, J. V.; Izmaylov, A. F.; Sonnenberg, J. L.; Williams-Young, D.; Ding, F.; Lipparini, F.; Egidi, F.; Goings, J.; Peng, B.; Petrone, A.; Henderson, T.; Ranasinghe, D.; Zakrzewski, V. G.; Gao, J.; Rega, N.; Zheng, G.; Liang, W.; Hada, M.; Ehara, M.; Toyota, K.; Fukuda, R.; Hasegawa, J.; Ishida, M.; Nakajima, T.; Honda, Y.; Kitao, O.; Nakai, H.; Vreven, T.; Throssell, K.; Montgomery, Jr., J. A.; Peralta, J. E.; Ogliaro, F.; Bearpark, M. J.; Heyd, J. J.; Brothers, E. N.; Kudin, K. N.; Staroverov, V. N.; Keith, T. A.; Kobayashi, R.; Normand, J.; Raghavachari, K.; Rendell, A. P.; Burant, J. C.; Iyengar, S. S.; Tomasi, J.; Cossi, M.; Millam, J. M.; Klene, M.; Adamo, C.; Cammi, R.; Ochterski, J. W.; Martin, R. L.; Morokuma, K.; Farkas, O.; Foresman, J. B.; Fox, D. J. *Gaussian 16, Revision C.01*; Gaussian, Inc.: Wallingford CT.
(68) Yanai, T.; Tew, D. P.; Handy, N. C. A New Hybrid Exchange-Correlation Functional Using the Coulomb-Attenuating Method (CAM-B3LYP). *Chem. Phys. Lett.* **2004**, *393*, 51−57.
(69) Adamo, C.; Barone, V. Toward Reliable Density Functional Methods without Adjustable Parameters: The PBE0 Model. *J. Chem. Phys.* **1999**, *110* (13), 6158−6170.
(70) Vydrov, O. A.; Scuseria, G. E. Assessment of a Long-Range Corrected Hybrid Functional. *J. Chem. Phys.* **2006**, *125*, 234109.
(71) Zhao, Y.; Truhlar, D. G. The M06 Suite of Density Functionals for Main Group Thermochemistry, Thermochemical Kinetics, Noncovalent Interactions, Excited States, and Transition Elements: Two New Functionals and Systematic Testing of Four M06-Class Functionals and 12 Other Function. *Theor. Chem. Acc.* **2008**, *120*, 215−241.
(72) Cornell, W. D.; Cieplak, P.; Bayly, C. I.; Gould, I. R.; Merz, K. M.; Ferguson, D. M.; Spellmeyer, D. C.; Fox, T.; Caldwell, J. W.; Kollman, P. A. A Second Generation Force Field for the Simulation of Proteins, Nucleic Acids, and Organic Molecules. *J. Am. Chem. Soc.* **1995**, *117* (19), 5179−5197.
(73) Vreven, T.; Morokuma, K. Investigation of the $S_0 \rightarrow S_1$ Excitation in Bacteriorhodopsin with the ONIOM(MO:MM) Hybrid Method. *Theor. Chem. Acc.* **2003**, *109* (3), 125−132.
(74) Melaccio, F.; Del Carmen Marín, M.; Valentini, A.; Montisci, F.; Rinaldi, S.; Cherubini, M.; Yang, X.; Kato, Y.; Stenrup, M.; Orozco-Gonzalez, Y.; Ferré, N.; Luk, H. L.; Kandori, H.; Olivucci, M. Toward Automatic Rhodopsin Modeling as a Tool for High-Throughput Computational Photobiology. *J. Chem. Theory Comput* **2016**, *12* (12), 6020−6034.
(75) Andruniów, T.; Ferré, N.; Olivucci, M. Structure, Initial Excited-State Relaxation, and Energy Storage of Rhodopsin Resolved at the Multiconfigurational Perturbation Theory Level. *Proc. Natl. Acad. Sci. U. S. A.* **2004**, *101* (52), 17908−17913.
(76) Schaftenaar, G.; Vlieg, E.; Vriend, G. Molden 2.0: Quantum Chemistry Meets Proteins. *J. Comput. Aided Mol. Des* **2017**, *31* (9), 789−800.
(77) Heyes, C. D.; El-Sayed, M. A. Proton Transfer Reactions in Native and Deionized Bacteriorhodopsin upon Delipidation and Monomerization. *Biophys. J.* **2003**, *85* (1), 426−434.
(78) Mei, G.; Mamaeva, N.; Ganapathy, S.; Wang, P.; DeGrip, W. J.; Rothschild, K. J. Raman Spectroscopy of a near Infrared Absorbing Proteorhodopsin: Similarities to the Bacteriorhodopsin O Photointermediate. *PLoS One* **2018**, *13* (12), No. e0209506.
(79) Heyes, C. D.; El-Sayed, M. A. The Role of the Native Lipids and Lattice Structure in Bacteriorhodopsin Protein Conformation and Stability as Studied by Temperature-Dependent Fourier Transform-Infrared Spectroscopy. *J. Biol. Chem.* **2002**, *277* (33), 29437−29443.
(80) Wu, S.; El-Sayed, M. A. CD Spectrum of Bacteriorhodopsin: Best Evidence against Exciton Model. *Biophys. J.* **1991**, *60* (1), 190−197.
(81) Ebrey, T. G.; Becher, B.; Mao, B.; Kilkbride, P. Exciton Interactions and Chromophore Orientation in the Purple Membrane. *J. Mol. Biol.* **1977**, *112*, 377−397.
(82) Grotjahn, R.; Furche, F.; Kaupp, M. Importance of Imposing Gauge Invariance in Time-Dependent Density Functional Theory Calculations with Meta-Generalized Gradient Approximations. *J. Chem. Phys.* **2022**, *157* (11), 111102.
(83) Gozem, S.; Johnson, P. J. M.; Halpin, A.; Luk, H. L.; Morizumi, T.; Prokhorenko, V. I.; Ernst, O. P.; Olivucci, M.; Miller, R. J. D. Excited-State Vibronic Dynamics of Bacteriorhodopsin from Two-Dimensional Electronic Photon Echo Spectroscopy and Multiconfigurational Quantum Chemistry. *J. Phys. Chem. Lett.* **2020**, *11* (10), 3889−3896.
(84) Palombo, R.; Barneschi, L.; Pedraza-González, L.; Padula, D.; Schapiro, I.; Olivucci, M. Retinal Chromophore Charge Delocalization and Confinement Explain the Extreme Photophysics of Neorhodopsin. *Nat. Commun.* **2022**, *13* (1), 6652.
(85) Godoy-Gallardo, M.; Mas-Moruno, C.; Fernández-Calderón, M. C.; Pérez-Giraldo, C.; Manero, J. M.; Albericio, F.; Gil, F. J.; Rodríguez, D. Covalent Immobilization of HLf1−11 Peptide on a Titanium Surface Reduces Bacterial Adhesion and Biofilm Formation. *Acta Biomater* **2014**, *10* (8), 3522−3534.
(86) Altun, A.; Yokoyama, S.; Morokuma, K. Quantum Mechanical/Molecular Mechanical Studies on Spectral Tuning Mechanisms of Visual Pigments and Other Photoactive Proteins. *Photochem. Photobiol.* **2008**, *84* (4), 845−854.
(87) Bravaya, K.; Bochenkova, A.; Granovsky, A.; Nemukhin, A. An Opsin Shift in Rhodopsin: Retinal S0-S1 Excitation in Protein, in Solution, and in the Gas Phase. *J. Am. Chem. Soc.* **2007**, *129* (43), 13035−13042.
(88) Ernst, O. P.; Lodowski, D. T.; Elstner, M.; Hegemann, P.; Brown, L. S.; Kandori, H. Microbial and Animal Rhodopsins: Structures, Functions, and Molecular Mechanisms. *Chem. Rev.* **2014**, *114* (1), 126−163.
(89) Andersen, L. H.; Nielsen, I. B.; Kristensen, M. B.; El Ghazaly, M. O. A.; Haacke, S.; Nielsen, M. B.; Petersen, M. Å. Absorption of Schiff-Base Retinal Chromophores in Vacuo. *J. Am. Chem. Soc.* **2005**, *127* (35), 12347−12350.
(90) Hayashi, T.; Matsuura, A.; Sato, H.; Sakurai, M. Full-Quantum Chemical Calculation of the Absorption Maximum of Bacteriorhodopsin: A Comprehensive Analysis of the Amino Acid Residues Contributing to the Opsin Shift. *Biophysics (Japan)* **2012**, *8*, 115−125.

https://doi.org/10.1021/acs.jctc.4c01370
J. Chem. Theory Comput. 2025, 21, 3231−3245

(91) Duncan, W. R.; Stier, W. M.; Prezhdo, O. V. Ab Initio Nonadiabatic Molecular Dynamics of the Ultrafast Electron Injection across the Alizarin - TiO_2 Interface. *J. Am. Chem. Soc.* **2005**, *127* (21), 7941−7951.
(92) Abuabara, S. G.; Rego, L. G. C.; Batista, V. S. Influence of Thermal Fluctuations on Interfacial Electron Transfer in Functionalized TiO_2 Semiconductors. *J. Am. Chem. Soc.* **2005**, *127* (51), 18234−18242.
(93) Stier, W.; Duncan, W. R.; Prezhdo, O. V. Thermally Assisted Sub-10 Fs Electron Transfer in Dye-Sensitized Nanocrystalline TiO_2 Solar Cells. *Adv. Mater.* **2004**, *16* (3), 240−244.
(94) Rego, L. G. C.; Batista, V. S. Quantum Dynamics Simulations of Interfacial Electron Transfer in Sensitized TiO_2 Semiconductors. *J. Am. Chem. Soc.* **2003**, *125* (26), 7989−7997.
(95) Kondov, I.; Thoss, M.; Wang, H. Theoretical Study of Ultrafast Heterogeneous Electron Transfer Reactions at Dye-Semiconductor Interfaces: Coumarin 343 at Titanium Oxide. *J. Phys. Chem. A* **2006**, *110*, 1364−1374.
(96) Duncan, W. R.; Prezhdo, O. V. Theoretical Studies of Photoinduced Electron Transfer in Dye-Sensitized TiO_2. *Annu. Rev. Phys. Chem.* **2007**, *58*, 143−184.
(97) Iannone, F; Ambrosino, F; Bracco, G; De Rosa, M; Funel, A; Guarnieri, G; Migliori, S; Palombi, P; Ponti, G; Santomauro, G; Procacci, P. *International Conference on High Performance Computing & Simulation (HPCS)*; IEEE: Ireland, Dublin, 2019; 1051−1052.

https://doi.org/10.1021/acs.jctc.4c01370
J. Chem. Theory Comput. 2025, 21, 3231−3245